FERMILAB-Pub-03/333 October 2003

# Beam decelerations with variable momentum compaction in the Fermilab Antiproton Accumulator

D.P. McGinnis, G. Stancari*, S.J. Werkema

*Fermi National Accelerator Laboratory, Antiproton Source Department, Batavia, IL 60510, USA*

**Abstract**

For the study of charmonium resonances above and including the $\chi_{c0}$, Fermilab experiment E-835 required an intense and stochastically cooled antiproton beam with kinetic energies from 8 GeV (the injection energy of the Accumulator) down to 4 GeV. We developed a scheme in which the momentum compaction factor of the machine was changed as the antiprotons were decelerated, so that the energies of interest to the experiment were kept above transition. The scheme was used during the E-835 10-month run of the year 2000. Here we describe the design criteria, operational procedures and diagnostic tools we used to exploit the machine as an efficient antiproton decelerator. The machine performance during data taking is also discussed, in relation to the main experimental requirements.


*PACS:* 13.75.Cs; 14.40.Gx; 29.20.Dh; 29.27.Eg

*Keywords:* Lattice; Deceleration; Transition energy; Charmonium

## 1. Introduction

Charmonium experiment E-760 and its continuation, E-835, took data at the Fermilab Antiproton Accumulator in 1990–1991 and 1996–1997, respectively. They studied the electromagnetic decays of charmonium resonances formed in $\bar{p}p$ collisions between the antiproton beam and an internal hydrogen-gas jet target [1,2]. During both data taking periods, the transition energy of the machine corresponded to a center-of-mass energy ($\sqrt{s}$) of 3.4 GeV, near the $\chi_{c0}$ resonance. In order to reach the lower-laying states ($\eta_c$ and $J/\psi$), a transition-crossing scheme was used. Transition crossing can be inefficient, especially when decelerating intense beams.

During 1998–1999, in view of Tevatron Run II, the Accumulator underwent a major upgrade, which included improvements of the stochastic cooling system. As a consequence, the lattice of the machine was redesigned and the new transition energy was set at $\gamma_t = 6.3$ (corresponding to $\sqrt{s} = 3.6$ GeV) [4]. For E-835, this meant that practically all long-lived charmonium resonances (except the $\psi'$) lay below transition, as shown in Fig. 1 and Table 1.

*Corresponding author. Present address: Dipartimento di Fisica, Università di Ferrara, Via Paradiso 12, 44100 Ferrara, Italy. Tel.: +39-0532-974330; fax: +39-0532-762057.

*E-mail address:* stancari@fe.infn.it (G. Stancari).

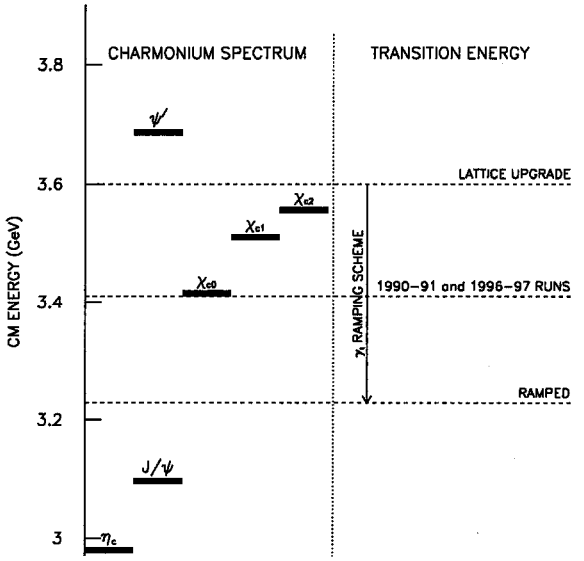


Fig. 1. Charmonium spectrum (representative resonances) and Accumulator transition energies translated into $\bar{p}p$ center-of-mass frame.

Table 1
Representative kinematic quantities for direct $\bar{p}p$ formation of charmonium resonances: center-of-mass energy $\sqrt{s}$, width $\Gamma$ [3], antiproton beam momentum $p$ and relativistic factor $\gamma$

| Resonance | Rest energy $Mc^2 = \sqrt{s}$ (GeV) | Width $\Gamma$ (MeV) | $p$ (GeV/$c$) | $\gamma$ |
|---|---|---|---|---|
| $\eta_c$ | 2.980 | 16 | 3.676 | 4.043 |
| $J/\psi$ | 3.097 | 0.087 | 4.066 | 4.447 |
| $\chi_{c0}$ | 3.415 | 16 | 5.192 | 5.624 |
| $\chi_{c1}$ | 3.511 | 0.9 | 5.550 | 5.999 |
| $\chi_{c2}$ | 3.556 | 2.1 | 5.725 | 6.183 |
| $\psi'$ | 3.686 | 0.30 | 6.232 | 6.716 |

For its year 2000 data-taking run, experiment E-835 decided to focus on the energy range between the $\chi_{c0}$ and the injection energy of the Accumulator (3.3 GeV $< \sqrt{s} <$ 4.3 GeV). It was therefore proposed to develop a scheme in which the transition energy is lowered as the antiprotons are decelerated, so that the experiment would always take data above transition.

In this paper, we describe the design and implementation of this scheme. After a brief description of the machine (Section 2), we discuss the lattice measurements that are necessary to build a model of its charged-particle optics (Section 3). In Section 4, the lattice design criteria are listed and the lattice calculations described, while Section 5 presents the operational procedures for their implementation. We conclude in Section 6 with an overview of the deceleration performance during the experiment's data-taking run.

## 2. The machine

The Antiproton Accumulator is roughly shaped like an equilateral triangle with flattened corners (Fig. 2); it has a total length of 474 m. Its main function is to accumulate antiprotons by momentum stacking, accomplished with the coordinated action of RF cavities and stochastic cooling systems. Here we summarize only those features relevant for the following discussion. For more information, see Refs. [5,6].

The ring is divided into six sectors of equal length, named A1–A6. The points joining two sectors are named A10 (found at the interface between A6 and A1), A20 (between A1 and A2), and so on. In each sector are 5 bending dipoles. All bending magnets are powered by a single bend bus (IB); each one is also equipped with an individual shunt. The dipoles are named after the quadrupole near which they are positioned. There are in fact 14 quadrupoles in each sector, powered by three main power supplies (QT, QDF and LQ) and equipped with individual and group shunts. In each sector are 3 sextupoles and 2 combined sextupole/octupole magnets. Nine horizontal and 24 vertical trim dipoles are used for orbit correction. The Accumulator is also equipped with 2 skew quadrupoles.

The beam is bunched and decelerated with RF system ARF-3 (2 cavities), located in the A5 sector. This cavity operates at the second harmonic of the revolution frequency ($h = 2$, $f_{RF} =$ 1.26 MHz at 8 GeV), with a peak voltage of 4 kV. While not accelerating or decelerating, ARF-3 is shorted and another $h = 2$ cavity, ARF-2, weakly bunches the beam (10 V) to clear trapped ions and to allow the beam-position monitor (BPM) system to sense the beam with its 48 horizontal and 42 vertical BPM detectors.

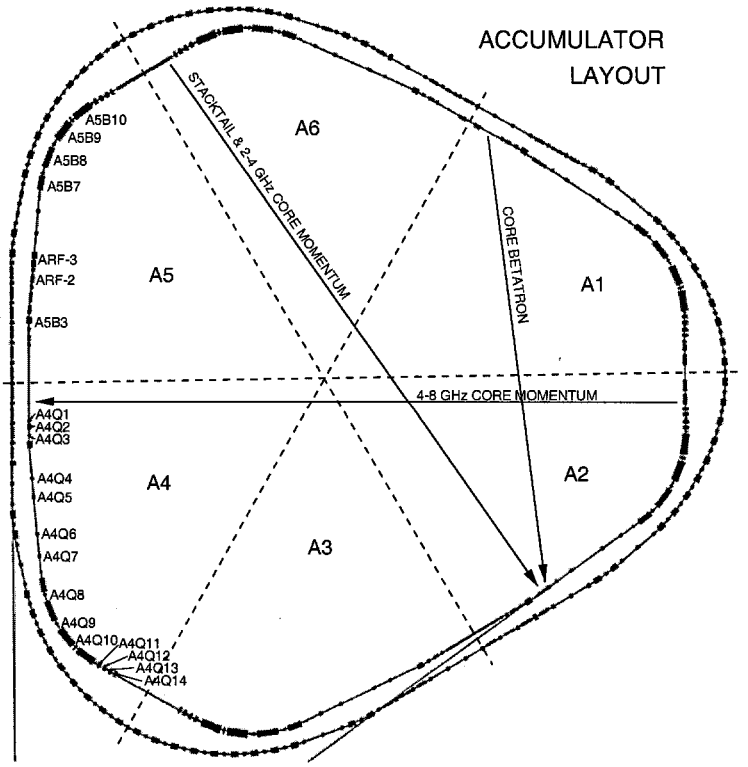


Fig. 2. Layout of the Antiproton Accumulator (inner ring).

There are three main stochastic cooling systems in the Accumulator. The stacktail momentum (2–4 GHz) is used for stacking; pickups are located in the A60 straight section, while kickers are positioned at A30. The core momentum is divided into two independent subsystems: 2–4 GHz, with fixed pickups at A60, and 4–8 GHz, with movable pickups at A20; kicker tanks are in the A30 and A50 straight sections, respectively. The core betatron systems (2–4 GHz and 4−8 GHz) control both horizontal and vertical emittance by sensing position errors in the A10 region and applying corrections at A30. Stochastic cooling dictates the main requirements on the machine lattice, as detailed in Section 4.

## 3. Lattice measurements

In this section, we summarize the methods used to measure the main lattice parameters. Knowledge of the 8-GeV lattice allowed us to build a machine model and provided a starting point for the dynamic lattices. The same measurements were performed as diagnostics during commissioning of the deceleration ramps. Some of the measurements, taken at representative beam momenta, were also necessary to determine the beam energy distribution for E-835's resonance analysis.

The slip factor $\eta$ was measured from the synchrotron frequency. After bunching the beam with ARF-3 at voltage $V_{RF}$, the signal from the longitudinal Schottky pickup was observed on a vector signal analyzer [7]. In Fig. 3, the central peak is the coherent bunched-beam signal at the 126th harmonic of the revolution frequency. The square and diamond-shaped markers indicate the largest synchrotron frequencies, which correspond to particles in the middle of the RF bucket. The synchrotron frequency $f_s$ is half of the frequency difference between the two markers (7.7 Hz in this case, with 85 V peak RF voltage). One can

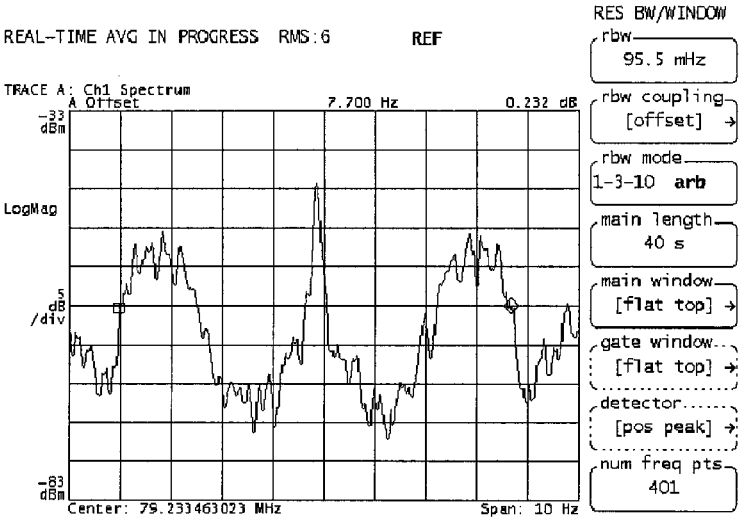


Fig. 3. Vector-signal-analyzer display of the synchrotron sidebands.

determine $\eta$ from the slope of $f_s^2$ vs $V_{RF}$ [8]:

$$f_s^2 = \left(-\frac{e\cos(\phi_s) f_{RF}^2}{2\pi h \beta^2 E}\right) \eta V_{RF}. \quad (1)$$

For non-accelerated beams, the synchronous phase $\phi_s$ is 0 below transition and $\pi$ above transition (our case); $\beta$ is the ratio between the synchronous particle's velocity and the speed of light, while $E$ is the synchronous energy; $h = 2$ is the RF harmonic number. The synchrotron frequency $f_s$ could be determined with a precision of 1%. The resulting uncertainty on $\eta$ was dominated by the error on the peak RF voltage (5%). An example of $\eta$ determination is shown in Fig. 4.

Once $\eta$ is known, the dispersion function at a certain location $s$ can be measured directly from the displacement $x'(s) - x(s)$ of beam bunched at frequency $f'_{RF}$ with respect to the orbit of beam bunched at $f_{RF}$ [8]:

$$D_x(s) = -\eta (x' - x) \frac{f_{RF}}{f'_{RF} - f_{RF}}. \quad (2)$$

The parameter $\gamma_t$ is usually obtained from $\eta$ through the relation [8]

$$\eta = \frac{1}{\gamma_t^2} - \frac{1}{\gamma^2}, \quad (3)$$

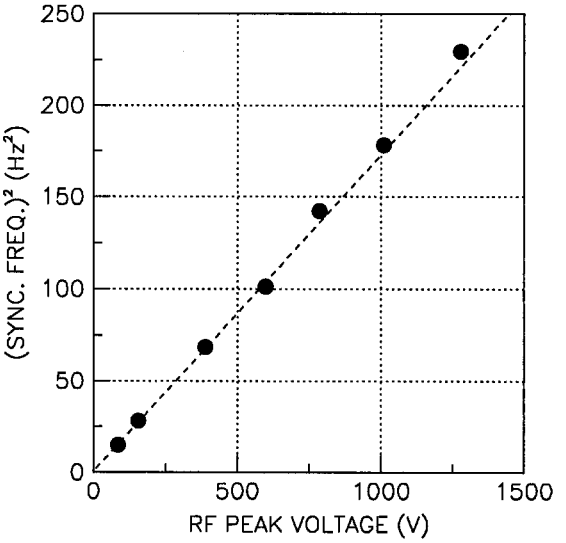


Fig. 4. Example of $\eta$ measurement from synchrotron frequency (25 August 1999 at 8 GeV).

where $\gamma$ is the particle's relativistic factor. The machine operates above transition if $\gamma > \gamma_t$ ($\eta > 0$), whereas the condition $\gamma = \gamma_t$ ($\eta = 0$) defines its transition energy. The value of $\gamma_t$ can also be measured independently of $\eta$. By varying the bend field and observing the corresponding revolution frequency change of the unbunched beam, one

obtains [8]:

$$\frac{\Delta f}{f} = \frac{1}{\gamma_t^2}\frac{\Delta B}{B}. \quad (4)$$

The value of $\gamma_t$ can be determined in this way with a precision of a few percent, the main uncertainty being the bending field $B$.

The betatron tunes $\nu_x$ and $\nu_y$ were measured to a precision of 0.001. Their fractional part was determined by comparing the frequency of the betatron sidebands to the beam revolution frequency. The frequency of the betatron sidebands was determined by spectrum analysis of the transverse Schottky signal [7]. The integer part of the tunes was evaluated from the number of orbit oscillations induced by a dipole kick. The Accumulator operated at $\nu_x = 6.685$ and $\nu_y = 8.695$.

We built a MAD [9] model of the lattice, which included the excitation curves measured at the Fermilab Magnet Test Facility for a subset of dipoles and quadrupoles before their installation. Since the information on the magnet strength vs current was not available for every magnet, we assigned a strength correction factor to each one of them. These factors were determined empirically by kicking the beam with each horizontal and vertical trim dipole and recording the corresponding orbit distortion. A best fit to the data using the model with the correction factors as free parameters yielded the correction factors themselves, which did not deviate from 1 by more than 2%. The most stringent constraint in this fitting procedure was the fractional value of the tunes, determined independently as described above. As a consequence, the $\beta$-functions were also determined from the model using the measured magnet strengths.

After building a reliable model and measuring the starting point of the deceleration (the 8-GeV lattice), we considered the design criteria for lattice during deceleration.

## 4. Design and calculation of the deceleration ramps

As the beam was decelerated from the starting 8-GeV kinetic energy, several device settings had to be updated by the front-end control system. The tables containing the settings for the magnet currents, RF cavity frequency and voltage, stochastic cooling parameters, etc. (a total of about 150 devices) as a function of time are referred to as *ramps*.

The bend-bus ramp was our reference ramp. It was taken from the 1996–1997 run and left unchanged. The RF frequency ramp was determined empirically during ramp development by minimizing orbit distortions due to energy shifts (see also Sections 5 and 6). The RF voltage ramp was designed to generate a constant bucket area.

The momentum compaction $\alpha \equiv 1/\gamma_t^2$ is the fractional deviation of the orbit length $C$ per unit fractional momentum deviation [8]:

$$\frac{\Delta C}{C} = \alpha\frac{\Delta p}{p}. \quad (5)$$

One can show that $\alpha$ is the average around the ring of the ratio between the dispersion function $D(s)$ and the radius of curvature of the orbit $\rho(s)$ [8]:

$$\alpha \equiv \frac{1}{\gamma_t^2} = \left\langle \frac{D}{\rho} \right\rangle_s. \quad (6)$$

In our case, the $\gamma_t$ reduction as a function of beam momentum was achieved by making $D$ less negative at dipoles AXB07 and more positive at dipoles AXB09 and AXB10. The value of $\gamma_t$, and therefore $\eta$ (Eq. (3)), is determined by the quadrupole currents, mainly by the LQ bus powering AXQ10, AXQ11, AXQ12, AXQ13 and AXQ14. The quadrupole-bus ramps were calculated to obtain the desired $\gamma_t$ ramp while fulfilling a series of lattice constraints. Even though $\gamma_t$ cannot be set by acting on a single device, we still refer to the '$\gamma_t$ ramp' for simplicity: it is a synonym of '$\gamma_t$ as a function of beam momentum'. The following considerations determined the $\gamma_t$ ramp:

- It had to start from $\gamma_t = 6.34$, the 8-GeV value.
- A small component of the uncertainty in the beam energy measurement was the effect of lattice differences between the reference energy and every other point where the energy was measured [1,10]. Operating with the same Accumulator lattice at all energies where accurate beam energy measurement was required eliminated this uncertainty. This

required that $\gamma_t$ reach its final minimum value above the $\psi'$ energy.

- The lowest energy of interest in the year 2000 E-835 run was that of the $\chi_{c0}$ resonance. The $\chi_{c0}$ has a width of 16 MeV; we required that the $\chi_{c0}$ resonance be at least 5 widths above transition. This imposed that the minimum value of $\gamma_t$ be below 5.3.
- The stochastic cooling had to work properly at all energies where E-835 data taking occurred. The mixing factor $M$, which is roughly the number of revolutions it takes to completely randomize the sample sensed by the pickup, is related to the slip factor $\eta$ through the following formula [11]:

$$M = \frac{f \ln 2}{W|\eta|(\sigma_p/p)}, \tag{7}$$

where $f$ is the average revolution frequency, $W$ is the system bandwidth (4 GHz), and $\sigma_p$ is the beam momentum spread. Near transition ($|\eta| \to 0$) the particles do not mix ($M \to \infty$), and the stochastic cooling cannot work. On the other hand, too far from transition the particles mix too quickly, even going from pickup to kicker ('bad mixing'): the information on their distribution detected by the pickup is useless at the kicker. In the Accumulator, experience dictates that the mixing factor should be in the interval $5 \leqslant M \leqslant 50$.

- We also required the value of $\eta$ to be large enough to avoid the onset of longitudinal instability. Longitudinal stability requires the longitudinal impedance $Z/h$ of the Accumulator to be less than the impedance threshold given by the Keil-Schnell stability criterion [8]:

$$\frac{Z}{h} < \left(\frac{Z}{h}\right)_{\text{thr}} \equiv \frac{2\pi F|\eta|\beta^2 E}{eI}\left(\frac{\sigma_p}{p}\right)^2, \tag{8}$$

where $F$ is a beam-shape form factor of the order of unity, $I$ is the beam current and $h$ is the harmonic number. The largest impedances in the Accumulator are the two ARF-3 cavities, which contribute approximately 1500 Ω per cavity at $h = 2$. Therefore we required the Keil-Schnell threshold to be greater than about 750 Ω. (We operated with one of the two ARF-3 cavities shorted.)

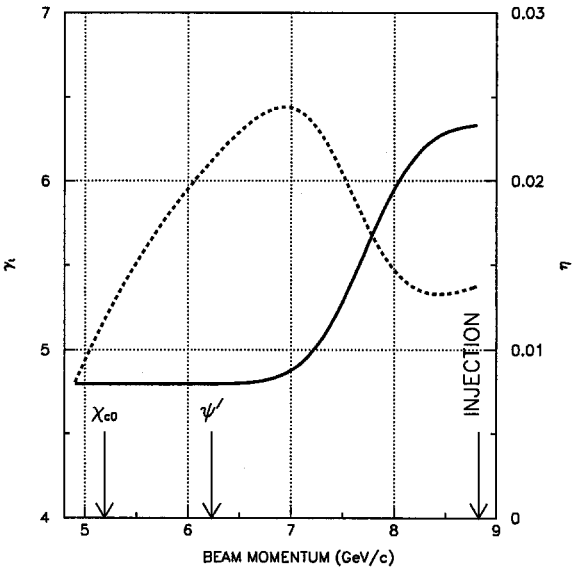


Fig. 5. Design $\gamma_t$ (solid) and $\eta$ (dashed) curves.

Based upon these considerations, we chose to shape the $\gamma_t$ ramp as in Fig. 5; the corresponding $\eta$ ramp is also shown. The resulting mixing factor and impedance threshold as a function of beam momentum are plotted in Fig. 6 for $I = 40$ mA and $\sigma_p = 2.0$ MeV/$c$.

Several other issues constrain the Accumulator lattice at any point in the deceleration ramps:

- Tunes should be constant, to avoid crossing of resonant lines.
- Chromaticity should be small (to keep tunes far from resonant lines) and positive (for transverse stability).
- Betatron phase advances between transverse cooling pickups and kickers should be within 20° of an odd multiple of 90°.
- For proper operation of the momentum cooling, the dispersion at the pickup should be approximately 10 m; whereas at the kicker it has to be not more than about 1 cm.
- Aperture considerations require the $\beta$-functions in both planes at the center of the zero-dispersion straight sections to be less than 8 m. However, to avoid degrading the sensitivity of the transverse pickups, the $\beta$-functions should be kept greater than about

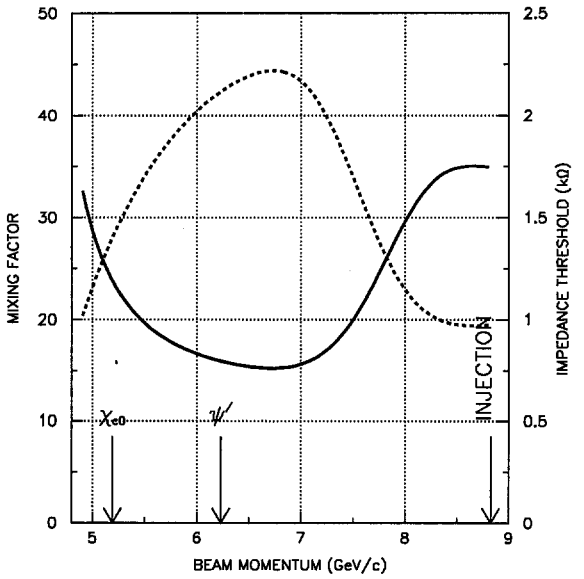


Fig. 6. Mixing-factor (solid) and impedance-threshold (dashed) curves resulting from the design $\gamma_t$ and $\eta$ ramps of Fig. 5, assuming a beam current $I = 40$ mA and a momentum spread $\sigma_p = 2.0$ MeV/$c$.

5 m. Elsewhere the $\beta$-functions should be as small as possible.

- The six-fold symmetry of the ring should be kept.

We wrote a computer program to calculate the ramps for all quadrupole buses and shunts. The energy span of interest, from 8 to 4 GeV, was subdivided into 64 break points. The lattice was calculated using the MAD model of the Accumulator. The above-mentioned lattice constraints were implemented in our software through a $\chi^2$, which represented the deviation of the current lattice parameters from their design values:

$$\chi^2 = \left[\frac{\gamma_t - \gamma_t^{(\text{design})}}{(\text{acceptable } \gamma_t \text{ error})}\right]^2 + \left[\frac{\nu_x - \nu_x^{(\text{design})}}{(\text{acceptable } \nu_x \text{ error})}\right]^2 + \cdots . \quad (9)$$

At each break point, the $\chi^2$ was minimized with respect to the bus and shunt currents, invoking MAD as a subroutine to recalculate the lattice after each bus-current adjustment. Once the lattice parameters had reached their desired values, the corresponding bus currents represented the starting point for the next energy break point.

At 8 GeV, magnets are starting to saturate. This was one of the main obstacles to the use of the Accumulator as a decelerator. Hysteresis effects had to be taken into account, based upon the available measurements of magnet-strengths as a function of current [12].

The output of the ramp calculations (i.e., all the bus and shunt currents at each of the 64 energy break points) was the starting point for actual ramp development.

## 5. Ramp development

The bulk of deceleration studies took place from the end of August until mid-October of 1999.

After measuring the 8-GeV lattice, we established the orbit of maximum aperture ($A_x = 10\pi$ mm mrad in the horizontal plane, $A_y = 11\pi$ mm mrad in the vertical plane).

The ramp-development plan was to bunch the beam with ARF-3 and to run the deceleration until beam losses became significant. The deceleration was then stopped and the necessary corrections were made and saved. The main causes of beam loss at this stage were tunes crossing resonant lines and orbit distortions. The latter were caused by dipole kicks or by a mismatch between the bend bus ramp and the RF frequency ramp. The process was repeated until the bottom of the ramp was reached. Because the studies were destructive and $\bar{p}$ stacking took hours, we used a proton beam instead of antiprotons. Protons circulated in the reverse direction with respect to antiprotons, so that the magnet polarity was the same. As hoped, it was not necessary to correct the magnet ramps after switching to forward antiprotons.

To monitor the tunes during deceleration, we built a simple tune-tracking system (Fig. 7), which proved very useful during commissioning. The betatron Schottky signal was down-converted (mixed) with a sine wave produced by a direct digital synthesizer (DDS) and sent to a vector signal analyzer (VSA). Since the Accumulator operated at a fractional tune of about 0.690, the

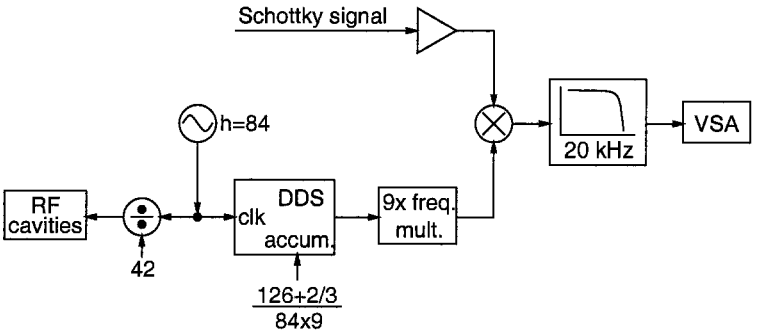


Fig. 7. Diagram of the tune-tracking system.

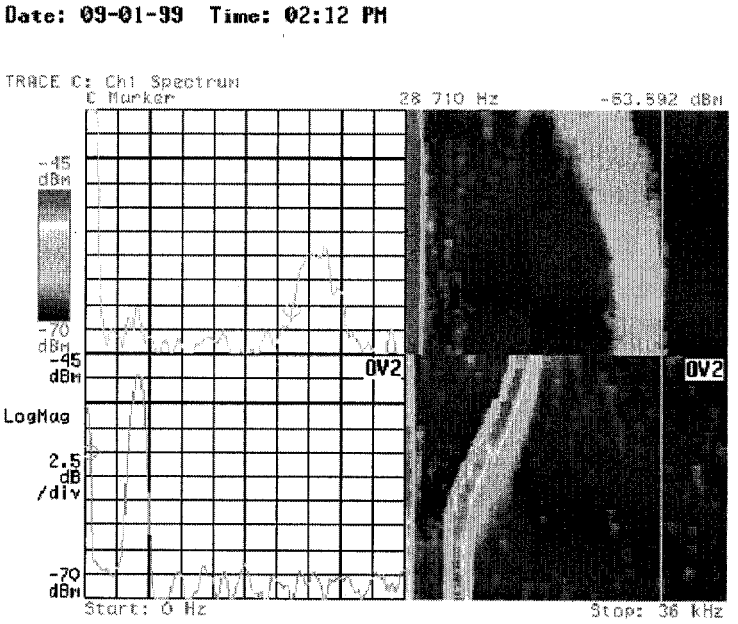


Fig. 8. On-line display of the machine tunes ('tune tracker').

closest resonance to avoid was the $\frac{2}{3}$. The desired fractional tune of the phase accumulator of the DDS was set to $\frac{2}{3}$, so that the down-converted frequency of 0 Hz corresponded to a tune of $\frac{2}{3}$. It might be of interest to the reader to observe the VSA display obtained during a deceleration (Fig. 8). The top two plots refer to the horizontal plane, while the bottom two are for the vertical plane. On the $x$-axis is the fractional part of the tune, from $\frac{2}{3} = 0.667$ to $\frac{5}{7} = 0.714$; the marker on the right-hand side plots (white vertical line) is placed at $\frac{7}{10} = 0.700$. The left-hand-side plots show the instantaneous signal spectra, whereas the right-hand-side ones show the evolution of the distributions, with time flowing from top-to-bottom as the beam was decelerated. In this particular case, the beam momentum decreased from 8779 MeV/$c$ to 8682 MeV/$c$, and the elapsed time was about 10 s. The deceleration was stopped about two-thirds of the way in the vertical time scale (where both tunes start to remain constant). Since chromaticity was constant, one expects the grey bands in the

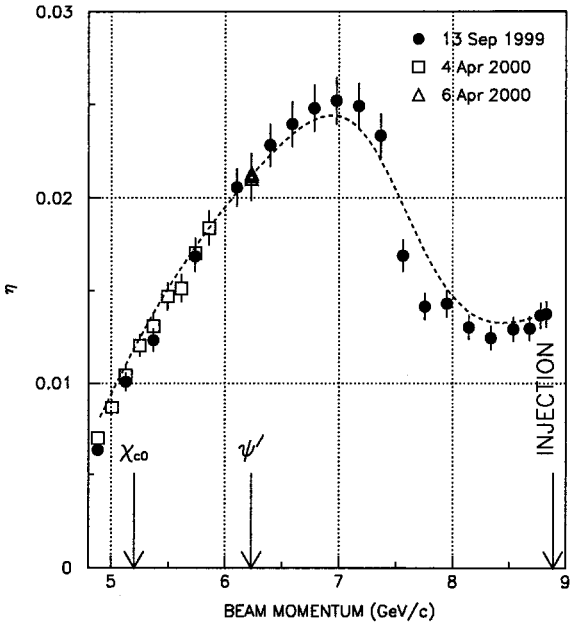


Fig. 9. Measured $\eta$ ramp compared with its design curve from Fig. 5. Three sets of synchrotron-frequency measurements have been performed: (a) after first ramp completion (circles); (b) after a $\beta$-function reduction (squares); and (c) check at the $\psi'$ energy, which is used by E-835 for energy calibration (triangles).

right-side plots to have constant width. Notice how, starting from about one-third of the way, the beam that crossed the $\frac{7}{10}$ resonance in the horizontal plane disappeared. At the same time, a corresponding drop in the beam current was observed.

Once beam survived the whole deceleration process, we ran several decelerations in small energy steps to correct the chromaticity, to suppress transverse coupling and to reduce the $\beta$ functions.

When the deceleration ramps were complete, we could measure $\eta$ and $\gamma_t$ at several energies and compare them with their design values. The results are shown in Fig. 9. They demonstrate the feasibility of the dynamic lattice scheme.

## 6. Application to E-835 data taking

The main experimental requirements for charmonium physics were beam intensity, energy stability and low momentum spread. A brief discussion of these requirements and how they were met is given in this section, together with an overview of deceleration procedures during the run.

Fermilab experiment E-835 was mainly devoted to high-resolution spectroscopy of $(c\bar{c})$ bound states. Charmonium resonances were directly formed in antiproton–proton annihilations, generated by interactions of the circulating antiproton beam with the internal hydrogen-gas jet target. The detector, located in the A50 region of the Accumulator, was especially sensitive to electromagnetic final states resulting from the decay of charmonium, such as, for instance, $\bar{p}p \to \chi_{c2} \to J/\psi + X \to e^+e^- + X$.

The resonance parameters (mass, width and peak cross-section) were measured with the energy scan technique. The antiproton beam energy was decreased in small steps across the resonance. At each energy point, the number of charmonium events ($J/\psi$ inclusive, for instance) was recorded. The numbers of events were fitted to the convolution of the beam energy spectra with a Breit-Wigner resonant cross section with free resonance parameters [13].

The beam requirements of the experiment were therefore rather demanding. First, let us consider beam intensity and the causes of antiproton losses. Since the cross sections of interest range between picobarns and nanobarns, instantaneous luminosities of about $2.5 \times 10^{31}$ cm$^{-2}$ s$^{-1}$ were required, corresponding to 90 events/nb/h. The jet target could reach densities $n_{\text{target}} = 3 \times 10^{14}$ atoms/cm$^3$; its shape limited the interaction region to a longitudinal thickness of $\Delta z = 6$ mm. Assuming a beam cross-section smaller than the target's and uniform densities, the luminosity is given by $\mathscr{L} = n_{\text{target}} \Delta z f N$, where $f = 0.6$ MHz is the revolution frequency and $N$ is the number of antiprotons. From this estimate, one obtains $N \geqslant 20 \times 10^{10}$ antiprotons.

During the year 2000 run, 8-GeV antiprotons were stacked at a rate of approximately $3 \times 10^{10}$ antiprotons/h, until a store of typically $40 \times 10^{10}$ particles was collected. (In the Accumulator, $10^{10}$ particles of continuous beam correspond to a beam current of 1 mA.) The beam was then

bunched, moved to the central orbit and cooled both transversely and longitudinally. The deceleration began by bunching the beam on the central orbit with ARF-3 at approximately 3 kV. The actual value depended on beam current and momentum spread; the beam had to be kept inside the RF bucket, especially when crossing the region where the slip factor $\eta$ was large. A few decelerations were also performed with variable voltage ramps. We estimate that RF leaks did not contribute to deceleration inefficiency for more than 2%. Another possibly important source of inefficiency was the transverse emittance growth caused by the deceleration. For this reason, when the target momentum was below 6.2 GeV/$c$, the deceleration was stopped around 6.3 GeV/$c$ (where $\eta$ was large) for extra beam cooling, after which the deceleration resumed. The whole deceleration process, from the end of stacking to the beginning of E-835 data taking, took approximately 3 h.

Figs. 10–12 show the deceleration efficiency for each stack vs time, initial beam current and target beam momentum. A total of 57 decelerations was performed. Two stacks were lost: one due to a power failure, the other due to beam instability. The mean overall deceleration efficiency, defined as the fraction of stacked antiprotons delivered to the experiment at the target energy, was 86%.

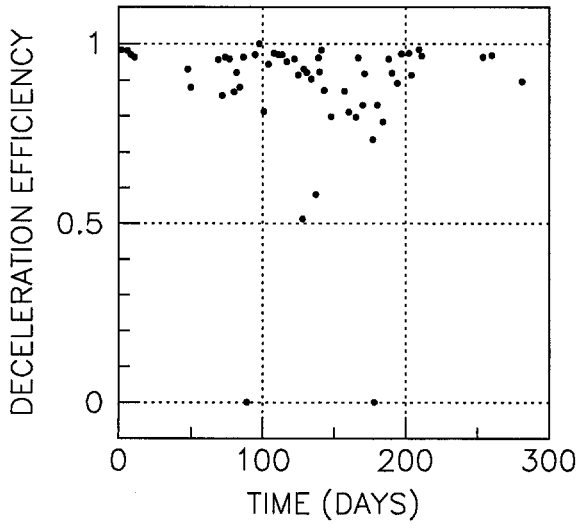


Fig. 10. Deceleration efficiency vs time.

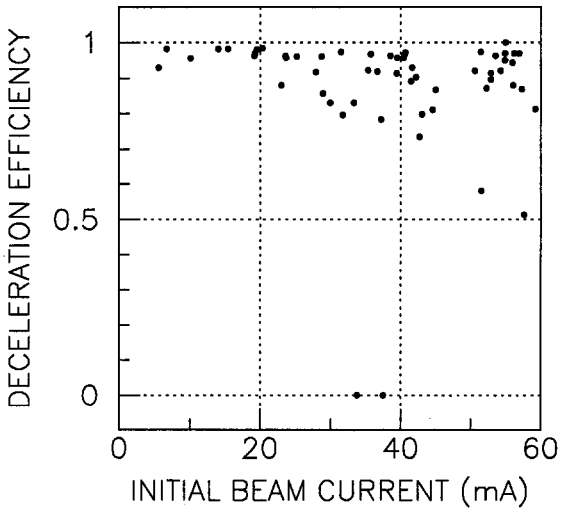


Fig. 11. Deceleration efficiency vs initial beam current (1 mA = $10^{10}$ particles).

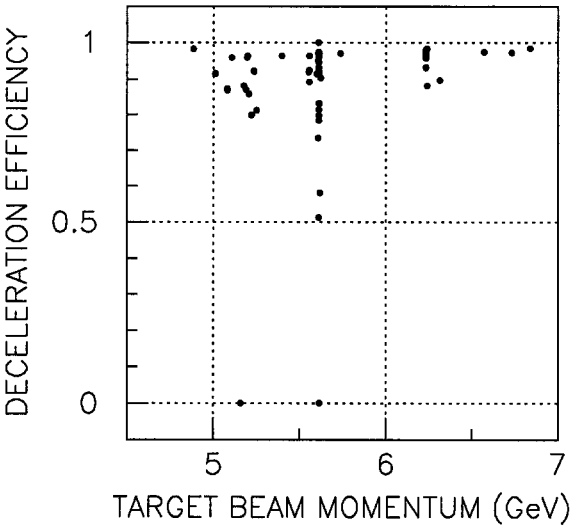


Fig. 12. Deceleration efficiency vs target beam momentum.

Besides a few inevitable equipment malfunctions, the main source of beam loss was transverse instability, both during deceleration and E-835 data taking. We observed sudden increases of the transverse emittances, often accompanied by beam loss. Sometimes emittance growth was triggered by opening of the jet target. The cause of the instability was not understood, but it was related to trapped ions [14] and to the fact that, during the

central part of the run, the tunes overlapped, with both fractional parts near 0.685. The tunes were in fact the parameters that were most sensitive to drifts of the magnet currents over time. After correcting the tunes along the ramps, the beam became stable again.

The experiment also required that the average beam energy be constant to within a few tens of kiloelectronvolts. To keep the beam at the desired energy a software control loop was used. An accelerator control application program determined the beam energy by monitoring the longitudinal Schottky spectrum and the BPM system. The beam energy was reported to the control system database at regular intervals (100 s) during data taking. The momentum stochastic cooling system employed during E-835 data taking used Palmer-type cooling, which consists of a pickup in a high-dispersion section of the machine. The horizontal position of the pickup array could be remotely controlled. This control allowed the stochastic cooling to cool to slightly different energies; its range was $\pm 25$ MeV about the central energy. The application program ran continually during data taking and it read periodically the energy of the beam from the control system database. The program compared the average energy of the beam to the desired energy and moved the array according to a first-order proportional-integral-derivative (PID) algorithm.

The momentum spread of the beam also plays an important role in the measurement of the parameters of narrow resonances. The widths of representative charmonium resonances are shown in Table 1. The relation between antiproton momentum spread $\Delta p$ and center-of-mass energy spread $\Delta\sqrt{s}$ is

$$\Delta\sqrt{s} = \frac{\beta m_p c^2}{\sqrt{s}} c(\Delta p) \approx \frac{1}{4} c(\Delta p). \tag{10}$$

The minimum attainable momentum spread was usually limited by longitudinal stability (Eq. (8)) rather than stochastic cooling power, even in the presence of a jet target. The energy spreads $(\Delta\sqrt{s})_{\mathrm{FWHM}}$ ranged between 0.3 MeV at the $\psi'$ and 1.6 MeV in the $\chi_{c0}$ region, for beam currents from 10 to 50 mA. Fig. 13 summarizes the data for a few representative E-835 runs; one can see that

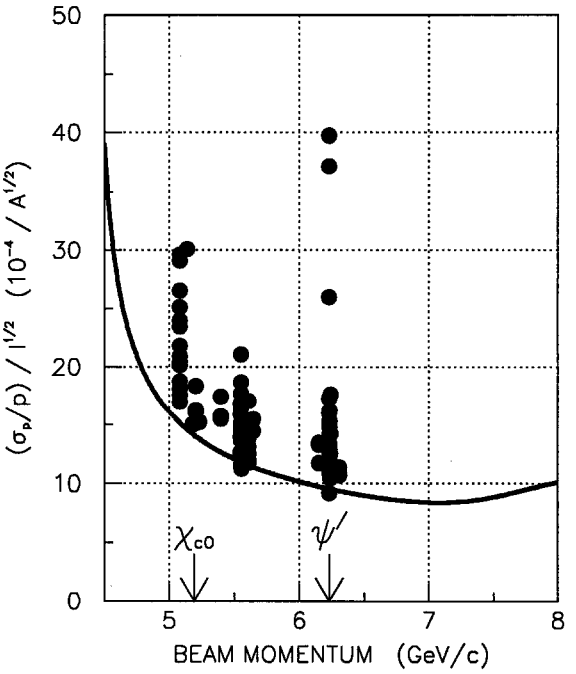


Fig. 13. Relative momentum spread per unit beam current vs target momentum. The continuous line represents the Keil-Schnell limit (Section 4).

the momentum spread was often pushed to the Keil-Schnell limit, causing some longitudinal instability, but usually no beam loss.

## 7. Conclusion

The overall performance of the deceleration ramps was very satisfactory. The feasibility of the dynamic lattice scheme has been shown and applied to the E-835 data taking. A tune adjustment was the only correction to the initial ramps that was necessary to make. They were in general very reliable and did not need further maintenance.


## Acknowledgements

We wish to thank our colleagues of the Antiproton Source Department. In particular, K. Gollwitzer and E. Harms participated in the ramp

development shifts; G. Garzoglio helped develop the energy-calculation software; M. Hu and A. Sondgeroth performed some of the decelerations. W. Marsh of the Accelerator Controls Department provided the computer code to run the ramps on the front-end control system. The support of the Accelerator Operations Group was invaluable during machine commissioning, ramp development, and E-835 data-taking run.

## References

[1] T.A. Armstrong, et al., Phys. Rev. D 47 (3) (1993) 772.

[2] M. Ambrogiani, et al., Phys. Rev. Lett. 83 (15) (1999) 2902.

[3] K. Hagiwara, et al., Phys. Rev. D 66 (2002) 010001 + URL pdg.lbl.gov.

[4] S. O'Day, M. Church, The Fermilab Accumulator ring lattice upgrade, in: M. Comyn, M.K. Craddock, M. Reiser, J. Thomson (Eds.), Proceedings of the 1997 Particle Accelerator Conference, Vol. 1, Vancouver, Canada, 1997, pp. 1006–1008.

[5] M.D. Church, J.P. Marriner, Annu. Rev. Nucl. Part. Sci. 43 (1993) 253.

[6] J.P. Morgan, The Antiproton Source Rookie Book, August 1999. URL www-bdnew.fnal.gov/pbar/documents/pbar_rookie_book.pdf

[7] D.W. Peterson, Schottky signal monitoring at Fermilab, in: E.S. McCrory (Ed.), Accelerator Instrumentation, Second Annual Workshop, Particles and Fields Series, Vol. 44, Fermi National Accelerator Laboratory, AIP Conference Proceedings No. 229, Batavia, IL, USA, 1990, p. 108.

[8] D.A. Edwards, M.J. Syphers, An Introduction to the Physics of High Energy Accelerators, Wiley, New York, 1993.

[9] H. Grote, F.C. Iselin, The MAD Program, CERN Program Library T5001, September 1994.

[10] S.J. Werkema, Precision measurement of the Accumulator beam energy, P-Bar Note 633, Fermilab, February 2000. URL www-bdnew.fnal.gov/pbar/documents/pbar-notes/pdf_files/pb633.pdf

[11] D. Möhl, G. Petrucci, L. Thorndahl, S. van der Meer, Phys. Rep. 58 (2) (1980) 73.

[12] G. Stancari, Parameterization of hysteresis effects in Accumulator quadrupole magnets, Technical Memo FERMILAB-TM-2094, Fermilab, October 1999.

[13] S. Bagnasco, et al., Phys. Lett. B 533 (2002) 237.

[14] S.J. Werkema, D.W. Peterson, P. Zhou, Transverse emittance growth in the Fermilab Antiproton Accumulator with high-current antiproton stacks, in: Proceedings of the 1993 Particle Accelerator Conference, Washington, DC, 1993, pp. 3573–3575.